

Morphology and Morphometry of Sub-kilometer Craters on the Nearside of Phobos and Implications for Regolith Properties*

Ryodo HEMMI^{1)†} and Hideaki MIYAMOTO^{1),2)}

¹⁾The University Museum, The University of Tokyo, Tokyo 113–0033, Japan

²⁾Department of Systems Innovation, The University of Tokyo, Tokyo 113–8656, Japan

Estimating the regolith properties of Phobos' surface is of critical importance for the landing and performance of the Martian Moons eXploration (MMX) sample return mission. Regolith physical properties such as strength, regolith thickness, and the presence of regolith layers are related to morphologies of superposing impact craters. However, the accurate depths of Phobos' sub-kilometer-diameter craters including irregularly shaped craters have not yet been fully characterized. Here, by using our high-resolution (20 m/pixel) digital elevation model of the nearside (or the sub-Mars side) of Phobos, we investigate the topographic profiles of the sub-kilometer craters. We confirm the presence of crater rims, and bowl-shaped, central-mound, and flat-floored crater geometries. The topography of one flat-floored crater is consistent with a boundary of regolith layers at a depth of ~160–180 meters. Morphometric measurements of 35 sub-kilometer craters show that their depth-to-diameter (d/D) ratios are in the range of 0.037 and 0.174 (mean value = 0.089, median value = 0.093). This suggests either a surface layer composed of rocky debris that effectively dissipates impact energy and causes a reduction in crater depth, or subsequent resurfacing events changed the original crater topography.

Key Words: Phobos, MMX, Space Science, Remote Sensing, Space Exploration

Nomenclature

d : crater depth, m

D : crater diameter, m

D_A : apparent crater diameter, m

t : regolith layer thickness, m

1. Introduction

For safe operation, determining the surface conditions of target bodies has been crucial to the planning of touchdown/landing for sample-return missions to small bodies (e.g., Hayabusa, Phobos-Grunt, Rosetta, Hayabusa2, OSIRIS-REx, etc.). For instance, Hayabusa2 spacecraft encountered an unprecedented amount of irregular-shaped boulders, ranging in 100s of meters to 10s of centimeters in scale, forming the entire rugged surface of the asteroid Ryugu,^{1–3)} forcing its first touchdown to be rescheduled to allow for additional engineering evaluations of all potential sampling sites. Additionally, the thruster firing at its first touchdown entrained a large number of particles, impairing the Hayabusa2 Optical Navigation Camera by decreasing its light sensitivity. This example illustrates how the dynamic behavior of regolith particles is of great importance when planning for future landing missions.

The Martian Moons eXploration (MMX) mission is planned to land on the surface of Phobos and collect more

than 10 g of samples from depths >2 cm at two separate sites.^{4,5)} High-resolution images (up to several meters per pixel), obtained by spacecraft orbiting Mars revealed that Phobos' surface is mostly covered by impact craters, grooves, pit chains, and boulders (Fig. 1). Craters and boulders smaller than the resolutions of previous images are expected. For the MMX spacecraft design, orbit planning, landing site selection, and landing operation, these densely-distributed topographic obstacles should be fully characterized using existing datasets before launch in 2024. In addition, the properties of regolith layer(s) (e.g., behavior of the surface materials when the lander foot pads and thruster plumes interact with the Phobos regolith, and the strength and packing density of regolith affecting stability of lander legs) should be estimated as accurately as possible.

In the case of Phobos, previous studies have identified two different spectral regions ("red and blue units"^{6–8)}; Fig. 2(a)), a range of morphologies of impact craters, or grooves. The cross-cutting and superposition relationships of these features strongly suggests that there were resurfacing events which produced regolith layers over time. Impact experiments and observations of lunar craters have shown that the contrast of mechanical properties between a loose regolith layer and its substrate affect the morphology of a superposed crater. In particular, changes in regolith thickness are to some extent responsible for changes in the crater morphology (i.e., bowl-shaped, flat-floored, central-mound, or concentric craters).^{9–11)} Crater morphology can therefore provide insights into the properties of subsurface structures (see, for example, Basilevsky et al.¹²⁾), which has not been well demonstrated due to the lack of accurate topography data of planetary surfaces other than the Moon and Mars.

© 2020 The Japan Society for Aeronautical and Space Sciences

*Presented at the 32nd International Symposium on Space Technology and Science, 15–21 June 2019, Fukui, Japan.

Received 30 June 2019; final revision received 29 January 2020; accepted for publication 18 March 2020.

†Corresponding author, hemmi@seed.um.u-tokyo.ac.jp

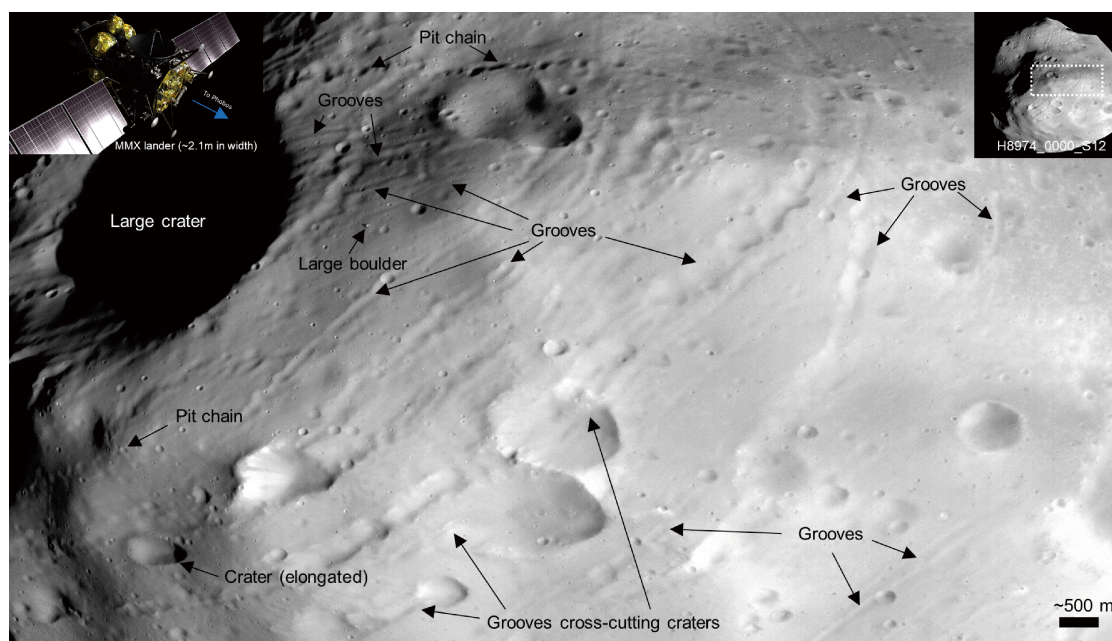


Fig. 1. Close-up view of geomorphological features on the Phobos' surface.
Part of HRSC image H8974_0000_S12. The upper left inset shows a drawing of the MMX spacecraft (Image credit: JAXA).

2. Impact Crater Morphology and Relation to Regolith Layering of Phobos

More than 9,000 craters larger than 50 m in diameter have been counted from the images of the Phobos surface.¹³⁾ Most of them exhibit a bowl-shaped geometry with different degrees of degradation (e.g., shallow crater depths, degraded crater rims, etc.). Some craters are associated with well-preserved elevated rims or rays (Fig. 2(b)), indicating that they were formed by impact rather than internal processes (e.g., drainage of regolith into fractured bedrock).

Morphologies of concentric, flat-floored, and central-mound interiors (e.g., Figs. 2(c)–2(e)) have been observed in craters with diameters ranging from 100s of meters to a few kilometers.^{12,14)} Though Thomas et al.¹⁴⁾ provided first-order estimates of the thickness of a loose surface layer above a mechanically stronger substrate from the diameter of flat-floored or concentric craters,¹¹⁾ their presence and geometry have not been confirmed by accurate topographic profiles using remote sensing data sets recently obtained. Therefore, for example, Basilevsky et al.¹²⁾ interpreted the crater in Fig. 2(e) as a central-mound crater, whereas, Thomas et al.¹⁴⁾ interpreted the same crater as being a flat-floor crater. Morphometric measurements of the craters with $D > 1$ km show that the larger crater depth-to-diameter (d/D) ratios are associated with a larger maximum steepness of the inner slopes.¹²⁾ This, as well as the presence of brighter or darker albedo streaks (Fig. 2(f)) and a landslide deposit (Fig. 2(g)), indicates downslope movement of loose materials in a surficial regolith layer.^{12,15,16)} These findings lead to a range of implications regarding the ages of geological events, the effects of shaking, the thickness of loose regolith layer and/or the characteristics of the subsurface materials.¹²⁾ The potential presence of an upper loose regolith layer would preferen-

tially affect the morphology of the smaller, shallower craters,¹⁷⁾ and yet, the d/D ratios of the Phobos sub-kilometer diameter craters are, so far, uncertain. Therefore, in this study, we extract topographic profiles of small craters with irregular shapes and measure the d/D ratios of craters with $D < \sim 1$ km to constrain the properties of regolith within ~ 100 m of the surface.

3. Data and Methods

3.1. High-resolution digital elevation model of Phobos

We use our recently developed digital elevation model (DEM) of Phobos derived from the application of bundle adjustment and triangulation to HiRISE stereo pair images (Fig. 3(a)).^{18–21)} Our DEM and its orthoimage are tied to a global HRSC Phobos dataset consisting of its own DEM and orthomosaic,^{22,23)} which are projected on a reference sphere having a 11.1 km radius (i.e., the DEM elevations are relative to this sphere) with equidistant cylindrical projection at pixel scales of ~ 20 m and ~ 6.56 m, respectively. With a vertical accuracy of ~ 4.17 m, our DEM covers the areas ranging from $\sim 60^\circ$ W to $\sim 60^\circ$ E (sub-Mars side) and from $\sim 30^\circ$ S to $\sim 70^\circ$ N, including the eastern rim of Stickney Crater, grooves, impact craters, and the red and blue units.²¹⁾

3.2. Measurements of crater diameters and depths

At least 1,000 sub-kilometer craters are present in the DEM coverage area, and we selected 35 craters with diameters from ~ 200 m to ~ 1 km (i.e., they can be resolved using $> 10 \times 10$ DEM pixels). Using the DEM and the orthoimage with the DEM-derived shaded relief map, we first mapped the crater rim-to-rim line passing through the center of each crater in the longitudinal direction (i.e., scale is true along the meridians in a plate carrée projection) (Fig. 3(b)). Topo-

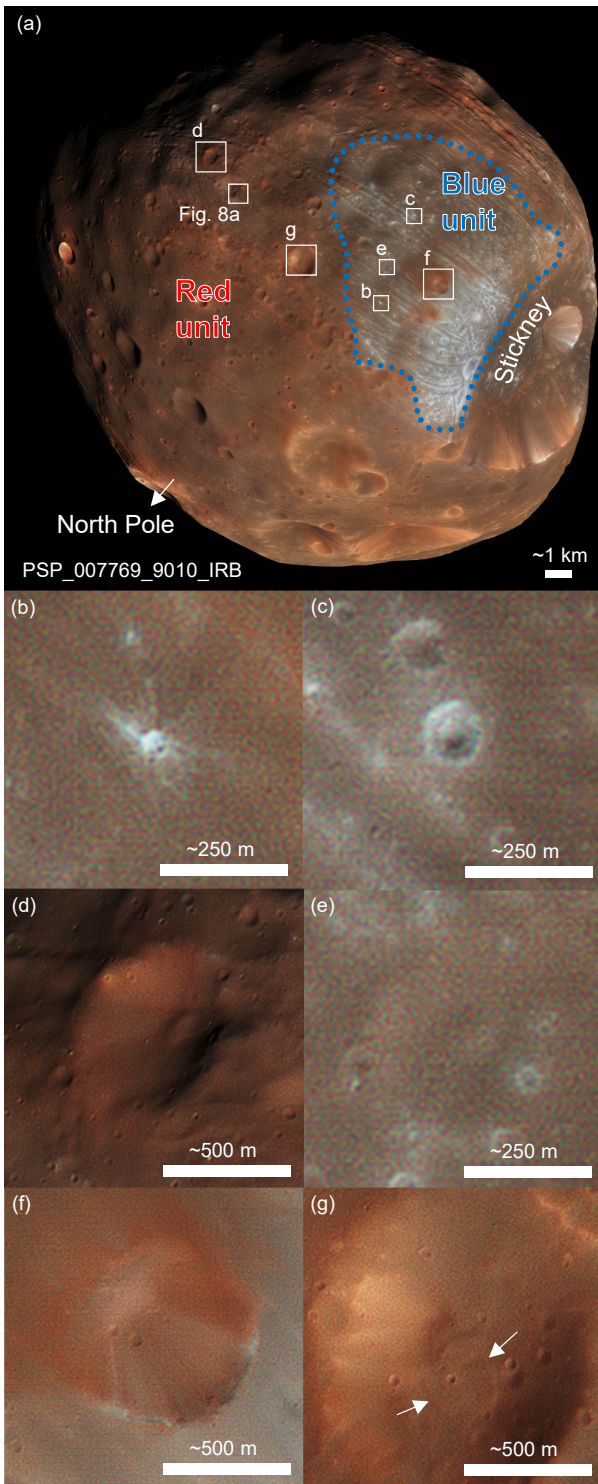


Fig. 2. Color-enhanced HiRISE image of Phobos (Image credit: NASA/JPL/University of Arizona).

(a) Red and blue units. Blue dotted outline depicts an approximate boundary of the blue unit. (b) Rayed crater. (c) Concentric crater. (d) Central-mound crater. (e) Flat-bottomed (or central-mound) crater. (f) Albedo streaks. (g) Landslide deposit (arrows).

graphic profiles were extracted for 35 craters in the DEM using the 3D Analyst tool in ArcGIS (ArcMap 10.2.2). In this study, the D value is defined as the length of a straight line connecting the northern and southern rim crests (i.e., the start and end of the profile), and the d value is calculated as the

length of the longest normal from the rim-to-rim line to the topographic profile. We then corrected the topography-related distortion of the D value, which comes from deviations between the actual surface and the reference sphere.²⁴⁾

4. Results

4.1. Topographic profiles of small craters

As shown in Fig. 4, we obtained topographic profiles of the six small craters (mostly less than 1 km in diameter). The most common morphology is a raised rim on the periphery of each crater, and the absence of the raised rim on one side (Fig. 4(d)) is identified as well. The profile of the crater previously interpreted as a central-mound (or a flat-floored) crater (Fig. 4(b)) exhibits a bowl-shape but has a slightly flat floor.^{12,14)} However, this observation does not exclude the potential presence of a central mound, which was not revealed using our DEM. While the DEM appears to provide an accurate geometry of a bowl-shaped crater (Fig. 4(a)), the elevation profile of a concentric crater (Fig. 4(c)) does not resolve the interior concentric depression seen in the imagery (Fig. 2(c)). This is probably because the vertical and horizontal resolutions of our DEM are insufficient to depict the detailed geometry. A flat-bottomed geometry associated with the crater in Fig. 4(d) is clearly shown in its topographic profile. Topographic profiles of the two central-mound craters (Figs. 4(e) and 4(f)) reveal obvious central mounds with heights reaching ~5 m to ~10 m.

The topography of the ~200 m-long landslide deposit and the associated scarp (Figs. 2(g), 4(d)) reveals its depleted zone/scarp (maximum slope of ~33 deg) on the crater wall and its accumulated zone (~2–4 m-thick landslide body) on the crater floor.^{12,25)}

4.2. Crater depths and diameters

Based on the topographic profiles extracted from the 35 sub-kilometer craters, we find that they have depths of 6.5 m to 136 m (mean = 44.2 m, median = 30.8 m, std. dev. = 35.9 m), and diameters from 177 m to 1,274 m (mean = 440.4 m, median = 376.9 m) (Fig. 5; Table 1). Their d/D ratios are in the range of 0.037 to 0.174 (mean = 0.089, median = 0.093, std. dev. = 0.039). There is no significant difference in the value of d between craters in the red and blue units; but this does not exclude the potential difference in d or d/D values between red and blue units for the sub-kilometer craters not measured in this study or the ones less than 100 m in diameter.

5. Discussion

5.1. Thickness of the regolith layers

The regolith of Phobos should have formed by the excavation, transportation, and mixing of materials at different depths by numerous impacts of different sizes. These processes could have left multi-layered structures within the Phobos regolith.¹⁷⁾ Impact experiments simulating complex craters formed on a loose surficial layer overlying a substrate showed that the ratio of their apparent crater diameters

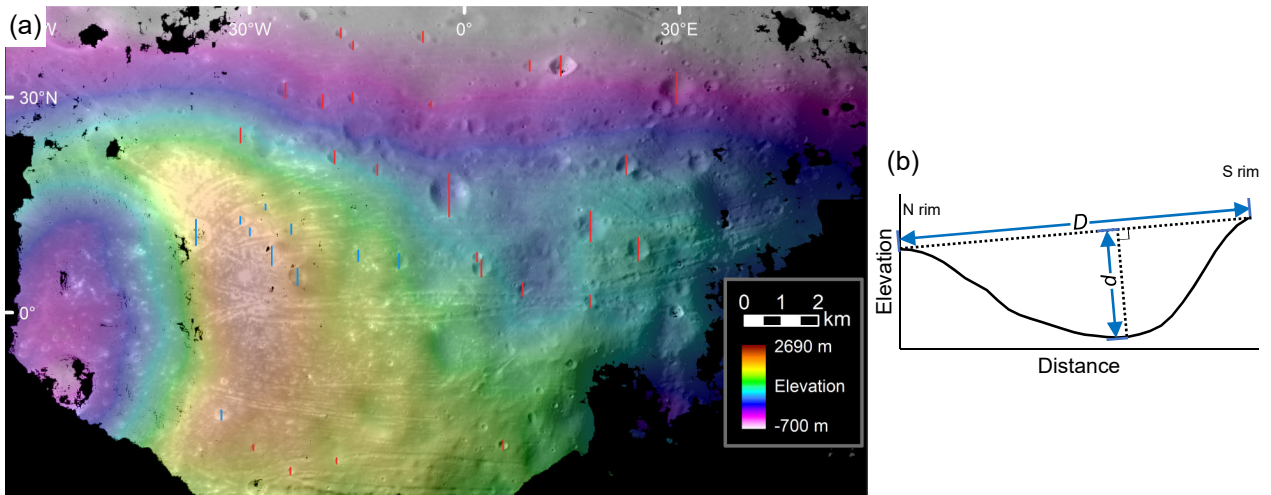


Fig. 3. Morphometric measurements of sub-kilometer craters.

(a) 35 sectional lines through each crater center. Red and blue line colors correspond to craters within the red and blue units, respectively. Base map is HiRISE DEM overlaid on its orthoimage. (b) Diagram showing lengths of d and D values determined from the topographic profile and the rimcrest-to-rimcrest line of each crater.

(i.e., planform diameter) to the layer thickness (D_A/t) can be related to the crater morphology: normal (bowl-shaped) craters at $D_A/t < 3.8$ – 4.2 , flat-bottomed craters (including central-mound craters) at 3.8 – $4.2 < D_A/t < 8$ – 10 , and concentric craters at $D_A/t > 8$ – 10 (Fig. 6).¹¹⁾ We tested this relationship using our high-resolution DEM and orthoimage of Phobos' nearside.

The largest crater measured in this study (Figs. 2(g) and 4(d)) has a flat floor, which may correspond to a boundary between an upper less-compressed (loose) layer and a more compacted substrate.¹¹⁾ From its topographic profile, the elevation difference between the crater floor and the surface outside the crater ($D_A = \sim 1,050$ m) is approximately 160 m–180 m. Treating this depth as the thickness of the overlying regolith layer gives $D_A/t = \sim 5.8$ – 6.6 , which falls within the expected range for flat-bottomed craters. If this analysis is true, then in at least one location, the maximum thickness of the regolith layer is larger than the previous estimate of the maximum layer depth of ~ 100 m derived from the morphology of grooves.^{12,14)} The other three topographic profiles of the ~ 400 m-scale craters (Figs. 4(b), 4(e), 4(f)) suggest ~ 20 m– 25 m as an estimated thickness of potential layer(s); however, their D_A/t values (~ 20 – 25) are greater than those expected for central-mound/flat-bottomed craters. Alternatively, the formation of these complex crater geometries can be explained by post-crater regolith migration and infilling into the crater floors (e.g., ejecta deposits originating from other sites, mass wasting at crater inner walls, etc.), decreasing crater depths and leaving either a flat floor or a central mound. Still, the thickness of the uppermost loose surficial layer may be less than several meters as suggested by the “painted-on” appearance of the red and blue units (Fig. 2(a)), small concentric crater (Fig. 2(c)) and surficial albedo streaks (Fig. 2(f)), which is difficult to determine precisely due to the resolution limit of our DEM (Fig. 4(c)).

5.2. Strengths of the upper loose surface layer

The strengths of regolith layers generally increase with depth, which is not quantitatively understood. The d/D ratios of the 35 sub-kilometer craters ($\sim 0.09 \pm 0.04$) are similar to those of sub-kilometer crater candidates on small (i.e., less than 1 km) asteroids such as Itokawa ($\sim 0.08 \pm 0.03$)²⁶⁾ and Ryugu ($\sim 0.07 \pm 0.03$),²⁷⁾ but are smaller than those of fresh craters on other large (i.e., several kilometers in size) asteroids (0.13 to 0.15).²⁶⁾ Basilevsky et al.¹²⁾ and Karachevtseva et al.²⁸⁾ found that the Phobos craters with $D > \sim 1$ km and $D > 1.5$ km have d/D ranges of ~ 0.02 – 0.21 and 0.04 – 0.21 , respectively (Fig. 7), both of which are larger than the d/D range of sub-kilometer craters (0.04–0.17). This suggests that there may be a change in regolith properties (e.g., spatial variations in regolith strength due to a fractured or rubble-pile interior) at the floors of the craters with diameters of ~ 1 km– 2 km (i.e., ~ 100 m– 300 m below the surrounding plains), which is consistent with the aforementioned layer boundary at depths of ~ 160 m– 180 m.

Moreover, as shown in Fig. 7, most of the craters analyzed with $D < 300$ m have d/D ratios well below 0.10 (i.e., depths $< \sim 30$ m). This may be ascribed to (i) a pre-crater regolith layer boundary (and the associated change in strength) causing the central-mound or flat-bottomed craters, (ii) a pre-existing layer loose rock debris within ~ 30 m of the surface that efficiently dissipates impact energy and results in very shallow craters, or (iii) post-crater processes that reduce crater depths.²⁹⁾ Figure 8(a) shows the profile of extremely shallow crater depths with a flat-floor geometry. Figure 8(b) represents a very gentle slope associated with downslope bright streaks on one side and a very steep slope on the other side. Both crater profiles are suggestive of later depositional events that reduce the depths of these small craters located within both red and blue units. Thus, we favor the two latter interpretations because the first interpretation is at odds with

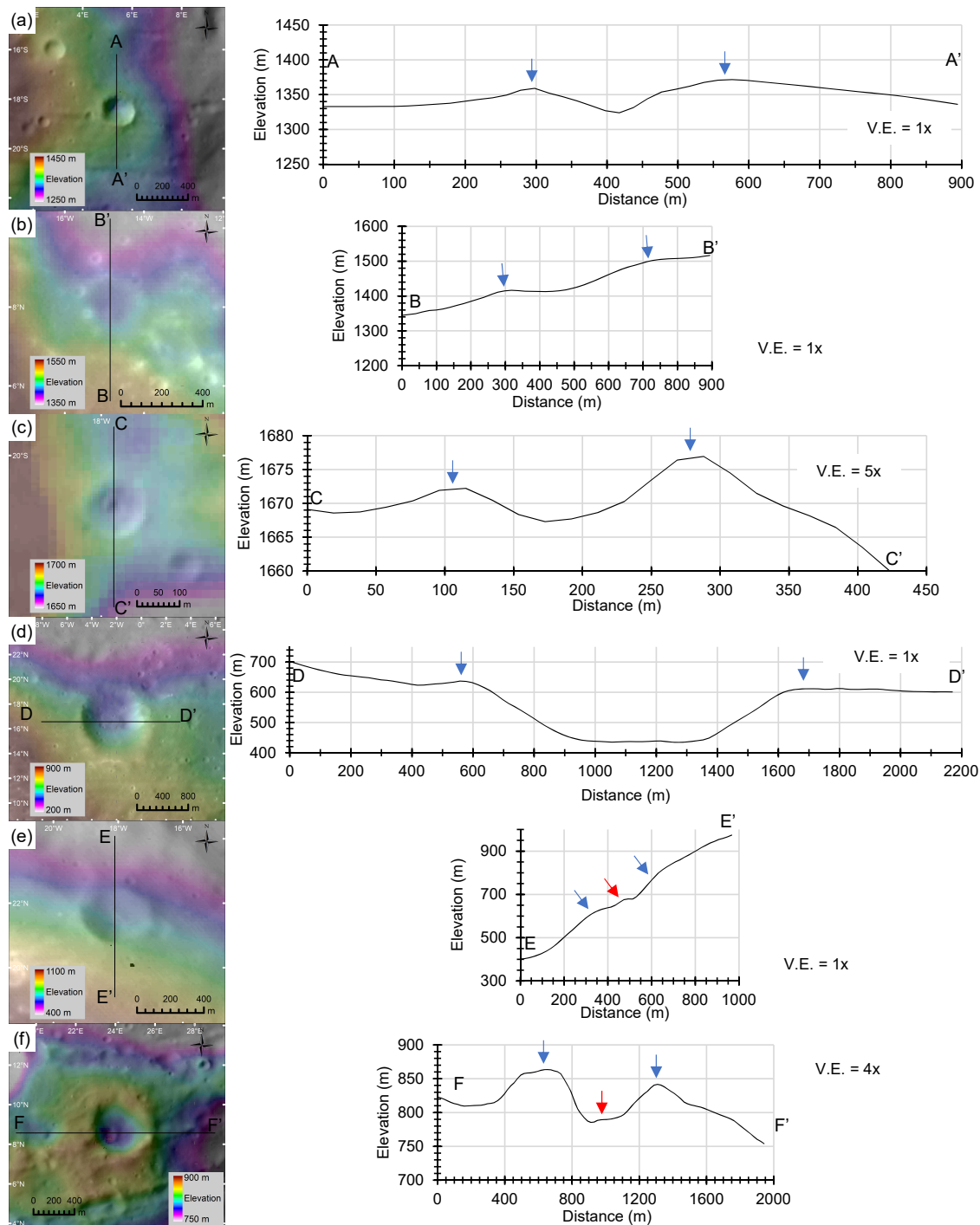


Fig. 4. Topographic profiles (right) for six small craters extracted from map-projected DEMs (left).

Positions of crater rims and central mounds are marked by blue and red arrows in plots, respectively. (a) Bowl-shaped crater. (b) Crater previously interpreted as a flat-floored/central-mound crater. The same crater in Fig. 2(e). (c) Concentric crater. The same crater in Fig. 2(c). (d) Flat-floored crater. The same crater in Fig. 2(g). (e) Central-mound crater. (f) Central-mound crater. The same crater in Fig. 2(d).

the above-described analyses of the D_A/t ratios of the ~ 400 m-sized complex craters.

6. Conclusion

Using the new high-resolution DEM, we extracted the topographic profiles and morphometric parameters of the sub-kilometer diameter craters of Phobos. Topographic profiles of the small flat-bottomed and central-mound craters

provide evidence for: (1) the presence of a boundary between the upper loose regolith layer with a thickness of ~ 160 m– 180 m and a more competent substrate, and (2) post-crater events reducing crater depths and forming flat floors or central mounds. Additionally, a pre-existing loose regolith layer with a thickness of $< \sim 30$ m may have caused a reduction in crater depth during crater formation. Crater depth-to-diameter ratios are comparable to craters on asteroids, which can be explained by a fragmental surface layer

effectively expending impact energy during excavation. In addition, the areas covered by the loose surface layers could have caused landslides on a local scale. These geomorphological aspects should be taken into consideration during the spacecraft design, landing site selection, and landing operation phases of the MMX mission.

To improve the precision of the estimates of this study, in the future, we will investigate (1) the extraction of morphologies of craters tens of meters in diameter, which must be related to a surface layer less than a few meters thick, by developing the much higher-resolution (i.e., several meters per pixel) DEM; (2) high-resolution topographic mapping of the sub-kilometer craters located outside of the study area (i.e., the anti-Mars, leading, trailing, and southern hemi-

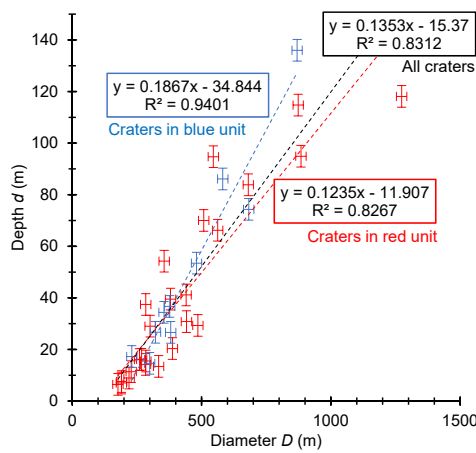


Fig. 5. Morphometric parameter plots of the 35 craters measured.

Red and blue colors represent craters in the red and blue units, respectively.

Table 1. Morphometric parameters of the 35 sub-kilometer craters.

Crater	Longitude	Latitude	d	D	d/D	Unit
00	-24.258	-21.847	11.4	228	0.050	Red
01	-17.834	-20.784	6.5	177	0.037	Red
02	9.126	34.186	15.5	284	0.055	Red
03	-5.778	38.101	29.0	301	0.096	Red
04	-17.238	38.775	16.1	260	0.062	Red
05	-24.951	30.489	30.8	442	0.070	Red
06	17.546	1.400	54.2	355	0.153	Red
07	8.157	2.839	39.5	380	0.104	Red
08	24.234	7.959	83.9	681	0.123	Red
09	29.679	30.224	94.9	884	0.107	Red
10	22.562	19.797	66.2	562	0.118	Red
11	17.594	11.150	114.8	874	0.131	Red
12	5.426	-18.439	37.4	284	0.132	Red
13	2.387	5.621	70.0	508	0.138	Red
14	-31.222	24.392	29.3	486	0.060	Red
15	-12.136	19.761	13.4	334	0.040	Red
16	-29.450	-18.673	7.6	191	0.040	Red
17	-33.900	-14.045	34.4	355	0.097	Blue
18	-14.815	7.432	26.6	381	0.070	Blue
19	13.462	33.777	94.7	546	0.174	Red
20	-4.613	28.934	7.0	190	0.037	Red
21	-15.626	29.676	14.2	283	0.050	Red
22	-15.527	37.088	9.0	220	0.041	Red
23	-19.756	29.165	20.3	387	0.053	Red
24	1.766	7.483	16.2	268	0.060	Red
25	-9.101	6.565	53.5	481	0.111	Blue
26	-23.294	4.744	86.1	582	0.148	Blue
27	-2.144	15.032	118.1	1274	0.093	Red
28	-18.103	21.287	41.1	440	0.093	Red
29	-37.448	11.573	136.0	869	0.156	Blue
30	-24.152	11.258	36.7	377	0.097	Blue
31	-26.863	7.169	74.3	682	0.109	Blue
32	-31.262	12.653	14.6	299	0.049	Blue
33	-29.943	10.959	26.7	322	0.083	Blue
34	-27.738	14.458	17.3	230	0.075	Blue

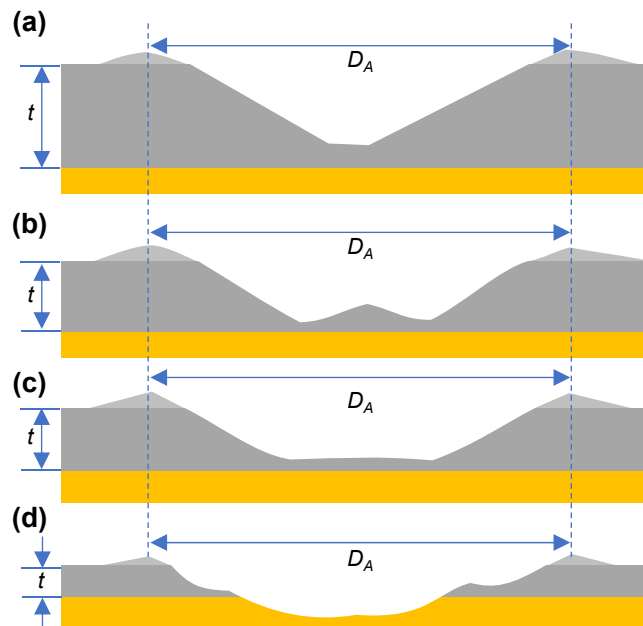


Fig. 6. Diagram showing the cross-sections of normal and complex craters formed on the loose unconsolidated layer (gray) overlying cohesive substrate (orange), which relates an apparent crater diameter of crater (D_A) to the layer thickness (t). Redrawn from Quaide and Oberbeck (1968).¹¹⁾

(a) Bowl-shaped crater ($D_A/t < 3.8-4.2$). (b) Central-mound crater ($3.8-4.2 < D_A/t < 8-10$). (c) Flat-bottomed crater ($3.8-4.2 < D_A/t < 8-10$). (d) Concentric crater ($D_A/t > 8-10$).

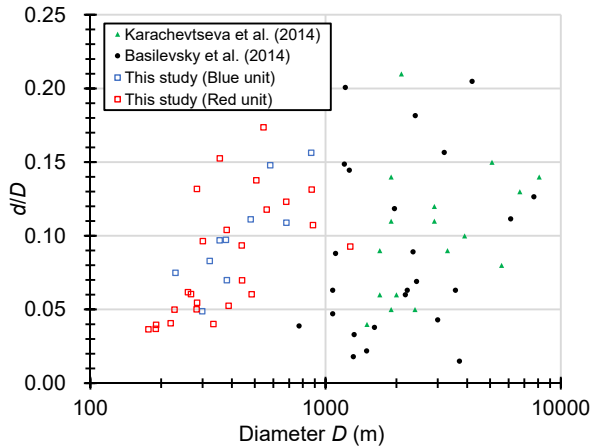


Fig. 7. Comparison of d/D ratios between the sub-kilometer craters and the previously-studied larger craters ($D > 1$ km).

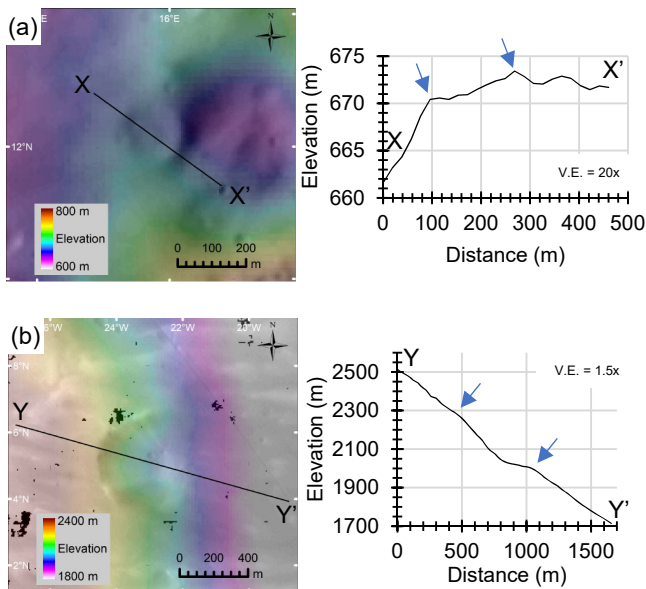


Fig. 8. Profiles of sub-kilometer craters with decreased crater depths.

(a) A flat-floored crater with very shallow interior. This crater is located within the red unit. (b) A crater with bright streaks on its western slope (Fig. 2(f)) showing an asymmetry of its interior profile. This crater is located within the blue unit.

spheres, and higher-latitude areas); and (3) integrating the morphometric measurements of the small craters, grooves, and other features (e.g., grooves, pit chains, albedo streams, etc.), including those automatically identified by MMX's TENG00/OROCHI images with lossy compression,³⁰ into a criteria or a hazard risk map based on regolith property estimates and a dynamic slope map for evaluating the safety of prospective landing sites.

Acknowledgments

We are grateful to an anonymous referee for his/her helpful comments. We wish to express our sincere appreciation to the MMX Landing Operation Working Team (LOWT), the TOKYO DOME CORPORATION, and the NTT DATA Corporation for their great support. We also thank Dr. Reid Parsons for his helpful comments on the manuscript.

References

- 1) Sugita, S., Honda, R., Morota, T., Kameda, S., Sawada, H., Tatsumi, E., Yamada, M., Honda, C., Yokota, Y., Kouyama, T., Sakatani, N., Ogawa, K., Suzuki, H., Okada, T., Namiki, N., Tanaka, S., Iijima, Y., Yoshioka, K., Hayakawa, M., Cho, Y., Matsuoka, M., Hirata, N., Miyamoto, H., Domingue, D., Hirabayashi, M., Nakamura, T., Hiroi, T., Michikami, T., Michel, P., Ballouz, R. L., Barnouin, O. S., Ernst, C. M., Schröder, S. E., Kikuchi, H., Hemmi, R., Komatsu, G., Fukuhara, T., Taguchi, M., Arai, T., Senshu, H., Demura, H., Ogawa, Y., Shimaki, Y., Sekiguchi, T., Müller, T. G., Hagermann, A., Mizuno, T., Noda, H., Matsumoto, K., Yamada, R., Ishihara, Y., Ikeda, H., Araki, H., Yamamoto, K., Abe, S., Yoshida, F., Higuchi, A., Sasaki, S., Oshigami, S., Tsuruta, S., Asari, K., Tazawa, S., Shizugami, M., Kimura, J., Otsubo, T., Yabuta, H., Hasegawa, S., Ishiguro, M., Tachibana, S., Palmer, E., Gaskell, R., Le Corre, L., Jaumann, R., Otto, K., Schmitz, N., Abell, P. A., Barucci, M. A., Zolensky, M. E., Vilas, F., Thuillet, F., Sugimoto, C., Takaki, N., Suzuki, Y., Kamiyoshihara, H., Okada, M., Nagata, K., Fujimoto, M., Yoshikawa, M., Yamamoto, Y., Shirai, K., Noguchi, R., Ogawa, N., Terui, F., Kikuchi, S., Yamaguchi, T., Oki, Y., Takao, Y., Takeuchi, H., Ono, G., Mimasu, Y., Yoshikawa, K., Takahashi, T., Takei, Y., Fujii, A., Hirose, C., Nakazawa, S., Hosoda, S., Mori, O., Shimada, T., Soldini, S., Iwata, T., Abe, M., Yano, H., Tsukizaki, R., Ozaki, M., Nishiyama, K., Saiki, T., Watanabe, S., and Tsuda, Y.: The Geomorphology, Color, and Thermal Properties of Ryugu: Implications for Parent-Body Processes, *Science*, **364** (2019), eaaw0422.
- 2) Watanabe, S., Hirabayashi, M., Hirata, N., Noguchi, R., Shimaki, Y., Ikeda, H., Tatsumi, E., Yoshikawa, M., Kikuchi, S., Yabuta, H., Nakamura, T., Tachibana, S., Ishihara, Y., Morota, T., Kitazato, K., Sakatani, N., Matsumoto, K., Wada, K., Senshu, H., Honda, C., Michikami, T., Takeuchi, H., Kouyama, T., Honda, R., Kameda, S., Fuse, T., Miyamoto, H., Komatsu, G., Sugita, S., Okada, T., Namiki, N., Arakawa, M., Ishiguro, M., Abe, M., Gaskell, R., Palmer, E., Barnouin, O. S., Michel, P., French, A. S., McMahon, J. W., Scheeres, D. J., Abell, P. A., Yamamoto, Y., Tanaka, S., Shirai, K., Matsuoka, M., Yamada, M., Yokota, Y., Suzuki, H., Yoshioka, K., Cho, Y., Nishikawa, N., Sugiyama, T., Kikuchi, H., Hemmi, R., Yamaguchi, T., Ogawa, N., Ono, G., Mimasu, Y., Yoshikawa, K., Takahashi, T., Takei, Y., Fujii, A., Hirose, C., Iwata, T., Hayakawa, M., Hosoda, S., Mori, O., Sawada, H., Shimada, T., Soldini, S., Yano, H., Tsukizaki, R., Ozaki, M., Iijima, Y., Ogawa, K., Fujimoto, M., Ho, T. M., Moussi, A., Jaumann, R., Bibring, J. P., Krause, C., Terui, F., Saiki, T., Nakazawa, S., and Tsuda, Y.: Hayabusa2 Arrives at the Carbonaceous Asteroid 162173 Ryugu—A Spinning Top-Shaped Rubble Pile, *Science*, **364** (2019), pp. 268–272.
- 3) Michikami, T., Honda, C., Miyamoto, H., Hirabayashi, M., Hagermann, A., Irie, T., Nomura, K., Ernst, C. M., Kawamura, M., Sugimoto, K., Tatsumi, E., Morota, T., Hirata, N., Noguchi, T., Cho, Y., Kameda, S., Kouyama, T., Yokota, Y., Noguchi, R., Hayakawa, M., Hirata, N., Honda, R., Matsuoka, M., Sakatani, N., Suzuki, H., Yamada, M., Yoshioka, K., Sawada, H., Hemmi, R., Kikuchi, H., Ogawa, K., Watanabe, S.-i., Tanaka, S., Yoshikawa, M., Tsuda, Y., and Sugita, S.: Boulder Size and Shape Distributions on Asteroid Ryugu, *Icarus*, **331** (2019), pp. 179–191.
- 4) Kuramoto, K., Kawakatsu, Y., Fujimoto, M., and MMX Study Team: Martian Moons Exploration (MMX) Conceptual Study Results, 48th Lunar and Planetary Science Conference, The Woodlands, Texas, 2086, 2017.
- 5) Kuramoto, K., Kawakatsu, Y., Fujimoto, M., Genda, H., Imamura, T., Kameda, S., Matsumoto, K., Miyamoto, H., Morota, T., and Nagaoka, H.: Martian Moons Exploration (MMX) Conceptual Study Update, 49th Lunar and Planetary Science Conference, The Woodlands, Texas, 2143, 2018.
- 6) Murchie, S. and Erard, S.: Spectral Properties and Heterogeneity of Phobos from Measurements by Phobos 2, *Icarus*, **123** (1996), pp. 63–86.
- 7) Rivkin, A. S., Brown, R. H., Trilling, D. E., Bell, J. F., and Plassmann, J. H.: Near-Infrared Spectrophotometry of Phobos and Deimos, *Icarus*,

- 156 (2002), pp. 64–75.
- 8) Fraeman, A. A., Arvidson, R. E., Murchie, S. L., Rivkin, A., Bibring, J. P., Choo, T. H., Gondet, B., Humm, D., Kuzmin, R. O., Manaud, N., and Zabalueva, E. V.: Analysis of Disk-Resolved OMEGA and CRISM Spectral Observations of Phobos and Deimos, *J. Geophys. Res. Planets*, **117** (2012), E00J15.
 - 9) Wilcox, B. B., Robinson, M. S., Thomas, P. C., and Hawke, B. R.: Constraints on the Depth and Variability of the Lunar Regolith, *Meteorit. Planet. Sci.*, **40** (2005), pp. 695–710.
 - 10) Bart, G. D.: The Quantitative Relationship between Small Impact Crater Morphology and Regolith Depth, *Icarus*, **235** (2014), pp. 130–135.
 - 11) Quaide, W. L. and Oberbeck, V. R.: Thickness Determinations of the Lunar Surface Layer from Lunar Impact Craters, *J. Geophys. Res.*, **73** (1968), pp. 5247–5270.
 - 12) Basilevsky, A. T., Lorenz, C. A., Shingareva, T. V., Head, J. W., Ramsley, K. R., and Zubarev, A. E.: The Surface Geology and Geomorphology of Phobos, *Planet. Space Sci.*, **102** (2014), pp. 95–118.
 - 13) Salamunićar, G., Lončarić, S., Pina, P., Bandeira, L., and Saraiva, J.: Integrated Method for Crater Detection from Topography and Optical Images and the New PH9224GT Catalogue of Phobos Impact Craters, *Adv. Space Res.*, **53** (2014), pp. 1798–1809.
 - 14) Thomas, P. C., Veverka, J., Sullivan, R., Simonelli, D. P., Malin, M. C., Caplinger, M., Hartmann, W. K., and James, P. B.: Phobos: Regolith and Ejecta Blocks Investigated with Mars Orbiter Camera Images, *J. Geophys. Res. Planets*, **105** (2000), pp. 15091–15106.
 - 15) Shingareva, T. V. and Kuzmin, R. O.: Mass-Wasting Processes on the Surface of Phobos, *Solar Syst. Res.*, **35** (2001), pp. 431–443.
 - 16) Shi, X., Oberst, J., and Willner, K.: Mass Wasting on Phobos Triggered by an Evolving Tidal Environment, *Geophys. Res. Lett.*, **43** (2016), pp. 12,371–12,379.
 - 17) Ramsley, K. R. and Head, J. W.: Mars Impact Ejecta in the Regolith of Phobos: Bulk Concentration and Distribution, *Planet. Space Sci.*, **87** (2013), pp. 115–129.
 - 18) Beyer, R. A., Alexandrov, O., and McMichael, S.: The Ames Stereo Pipeline: NASA's Open Source Software for Deriving and Processing Terrain Data, *Earth Space Sci.*, **5** (2018), pp. 537–548.
 - 19) Hemmi, R. and Miyamoto, H.: Distribution, Morphology, and Morphometry of Circular Mounds in the Elongated Basin of Northern Terra Sirenum, Mars, *Prog. Earth Planet. Sci.*, **4** (2017), 26.
 - 20) Hemmi, R. and Miyamoto, H.: High-Resolution Topographic Analyses of Mounds in Southern Acidalia Planitia, Mars: Implications for Possible Mud Volcanism in Submarine and Subaerial Environments, *Geosciences*, **8** (2018), 152.
 - 21) Hemmi, R. and Miyamoto, H.: HiRISE Digital Elevation Model of Phobos: Implications for Morphological Analysis of Grooves, 50th Lunar and Planetary Science Conference, The Woodlands, Texas, 1759, 2019.
 - 22) Willner, K., Shi, X., and Oberst, J.: Phobos' Shape and Topography Models, *Planet. Space Sci.*, **102** (2014), pp. 51–59.
 - 23) Wählisch, M., Stooke, P. J., Karachevtseva, I. P., Kirk, R., Oberst, J., Willner, K., Nadejdina, I. A., Zubarev, A. E., Konopikhin, A. A., and Shingareva, K. B.: Phobos and Deimos Cartography, *Planet. Space Sci.*, **102** (2014), pp. 60–73.
 - 24) Kneissl, T., Schmedemann, N., Neesemann, A., Raymond, C. A., and Russell, C. T.: Crater Counting on Small Bodies—The Influence of Topography-Related Distortions, 45th Lunar and Planetary Science Conference, The Woodlands, Texas, 2398, 2018.
 - 25) Thomas, N., Stelter, R., Ivanov, A., Bridges, N. T., Herkenhoff, K. E., and McEwen, A. S.: Spectral Heterogeneity on Phobos and Deimos: HiRISE Observations and Comparisons to Mars Pathfinder Results, *Planet. Space Sci.*, **59** (2011), pp. 1281–1292.
 - 26) Hirata, N., Barnouin-Jha, O. S., Honda, C., Nakamura, R., Miyamoto, H., Sasaki, S., Demura, H., Nakamura, A. M., Michikami, T., Gaskell, R. W., and Saito, J.: A Survey of Possible Impact Structures on 25143 Itokawa, *Icarus*, **200** (2009), pp. 486–502.
 - 27) Cho, Y., Morota, T., Kanamaru, M., Ernst, C. M., Barnouin, O. S., Tatsumi, E., Hirabayashi, M., Otto, K. A., Schmitz, N., and Wagner, R. J.: Spatial Distribution and Morphology of Craters on Ryugu: Implications for Surface Processes on the C-Type Asteroid, 50th Lunar and Planetary Science Conference, The Woodlands, Texas, 1751, 2019.
 - 28) Karachevtseva, I. P., Oberst, J., Zubarev, A. E., Nadezhkina, I. E., Kokhanov, A. A., Garov, A. S., Uchaev, D. V., Uchaev, Dm. V., Malinnikov, V. A., and Klimkin, N. D.: The Phobos Information System, *Planet. Space Sci.*, **102** (2014), pp. 74–85.
 - 29) Melosh, H. J.: *Impact Cratering: a Geologic Process*, Oxford University Press, New York, 1989, pp. 82–84.
 - 30) Shimizu, Y., Kamiyoshihara, H., Niihara, T., and Miyamoto, H.: Experimental Study to Determine the Best Compression Ratio of High-Resolution Images of Small Bodies for Martian Moons eXploration Mission, *Trans. Jpn. Soc. Aeronaut. Space Sci.*, in press.

Tatsuaki Okada
Associate Editor